Acta Mech 227, 3087–3100 (2016)
DOI 10.1007/s00707-015-1543-8

ORIGINAL PAPER

Marco Antonio Meggiolaro · Jaime Tupiassú Pinho de Castro · Hao Wu

On the use of tensor paths to estimate the nonproportionality factor of multiaxial stress or strain histories under free-surface conditions

Received: 31 December 2014 / Revised: 14 September 2015 / Published online: 21 December 2015

Abstract Nonproportional (NP) strain hardening is caused by multiaxial load histories that induce variable principal stress/strain directions, activating cross-slip bands in several directions, due to the associated rotation of the maximum shear planes. This effect increases the strain-hardening behavior observed under proportional loads, those with fixed principal directions, and must be considered in multiaxial fatigue calculations, especially for materials with low stacking fault energy, such as austenitic stainless steels. NP hardening depends on the material and on the shape of the multiaxial load history path in a stress or strain diagram as well. It can be evaluated by a nonproportionality factor F_{NP} that varies from zero, for a proportional load history, to one, for a 90° out-of-phase tension–torsion loading with the same normal and effective shear amplitudes. Originally, F_{NP} was estimated from the aspect ratio of a convex enclosure that contains the load history path, such as an ellipse or a prismatic enclosure, but such convex enclosure estimates can lead to poor predictions of F_{NP}. Another approach consists on evaluating the shape of the six-dimensional (6D) path described by the six normal and shear components of the stress tensor, where the stress path contour is interpreted as a homogeneous wire with unit mass. The moment of inertia (MOI) tensor of this hypothetical wire is then calculated and used to estimate F_{NP}. The use of 6D stress paths to estimate F_{NP} is questionable, since 6D formulations implicitly include the effect of the hydrostatic stress, while NP hardening is caused by the deviatoric plastic straining, not by stresses alone or by their hydrostatic component. In this work, the NP factor F_{NP} of a multiaxial load history is estimated from the eigenvalues of the MOI tensor of the plastic strain path, which are associated with the accumulated plastic straining in the principal directions defined by the associated eigenvectors. The presented formulation assumes free-surface conditions, but allows a surface pressure, covering the conditions of most critical points, which indeed are located on free surfaces. Experimental results for 14 different tension–torsion multiaxial histories prove the effectiveness of the proposed method.

M. A. Meggiolaro (✉) · J. T. P. de Castro
Pontifical Catholic University of Rio de Janeiro, PUC-Rio, Rua Marquês de São Vicente 225, Rio de Janeiro, RJ 22451-900, Brazil
E-mail: meggi@puc-rio.br

J. T. P. de Castro
E-mail: jtcastro@puc-rio.br

H. Wu
School of Aerospace Engineering and Applied Mechanics, Tongji University, Siping Road 1239, Shanghai 200092, People's Republic of China
E-mail: wuhao@tongji.edu.cn

1 Introduction

Proportional multiaxial loadings cause isotropic strain-hardening effects that may cyclically harden or soften the material. Nonproportional (NP) multiaxial loadings, on the other hand, besides isotropic strain-hardening effects, may cause an additional effect called NP hardening, cross-hardening, or simply additional strain hardening. This effect depends on the multiaxial load history, by a nonproportionality factor F_{NP}, and on the material, by an NP or additional hardening constant α_{NP}, where $0 \leq \alpha_{\text{NP}} \leq 1$. Typically, the NP strain-hardening effect is high in austenitic stainless steels at room temperature (e.g., $\alpha_{\text{NP}} \cong 1$ for the 316 stainless steel under high plastic strain levels), medium in most carbon steels ($\alpha_{\text{NP}} \cong 0.3$ for a 1045 steel), and low in aluminum alloys ($\alpha_{\text{NP}} \cong 0$ for Al 7075). Table 1 shows typical values of α_{NP} for some metals.

Microstructurally, NP strain hardening is related to stacking faults, which are local regions of incorrect stacking of crystal planes [5,6]. Figure 1 shows stacking fault examples for HCP (hexagonal close-packed) and for FCC (face-centered cubic) lattices. HCP lattices superimpose the various atomic planes following a double sequence like *ab–ab–ab*. The stacking fault in the HCP lattice from Fig. 1(top) is caused by the plane arranged in the *c* configuration, causing an interruption of the stacking sequence of the crystal structure, which becomes *ab–ab–*$\underline{abc}$*–ab–ab*. FCC lattices, on the other hand, which usually follow a triple sequence *abc–abc–abc*, may present stacking faults from the local absence of such *c* configuration, as shown in the sequence *abc–abc–*$\underline{ab}$*–abc* in Fig. 1(bottom). Such faults cause the HCP lattice to become locally FCC in the $\underline{abc}$ plane sequence, while the FCC lattice locally becomes HCP in the $\underline{ab}$ region. These planar defects cause crystal lattice incompatibilities that prevent or impair dislocations from switching gliding planes, and thus affect their strain-hardening behavior.

Each of these crystallization faults is associated with a stacking fault energy (SFE) necessary to generate them, measured per unit area in J/m^2. Materials with low SFE can very easily develop large stacking faults. For instance, the FCC lattice of 316 stainless steels requires only 25 mJ per m^2 to generate them. Screw dislocations associated with plastic straining cannot easily cross-slip across such large stacking faults, even under relatively high stresses, due to the crystal lattice incompatibility. Hence, the slip bands generated by proportional loadings tend to remain planar. However, in the presence of NP loads, the changes in the principal

Table 1 Additional hardening coefficients α_{NP} for several materials [1–4]

Material	α_{NP}
316 stainless	0.75–1.0
304 stainless	0.5–1.0
304 stainless (650 °C)	0.3–0.4
SGV410	0.39
1045 steel	0.3
430 stainless	0.28
Inconel 718, S25C	0.2
Al 6061-T6	0.2
OFHC copper	0.16–0.3
42 CrMo steel	0.15
1 % Cr Mo-V, En15R steel	0.14
Al 1100, Al 7075	0.0

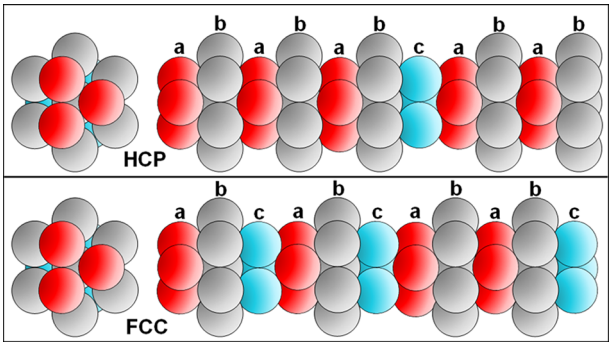

Fig. 1 HCP and FCC lattices with stacking faults

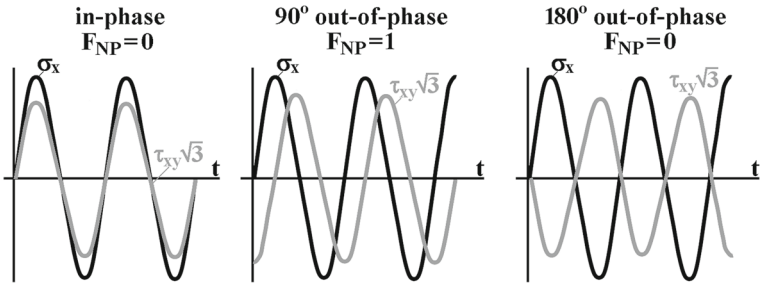

Fig. 2 In-phase, 90° out-of-phase and 180° out-of-phase tension–torsion histories

direction finally allow the activation of cross-slip bands in all directions. An increase in the hardening effect with respect to proportional loadings is thus expected, caused by the change in direction of the maximum shear planes, resulting in an additional hardening coefficient $\alpha_{NP} >> 0$.

On the other hand, stacking faults are rarely seen in materials with high SFE, such as in most aluminum alloys, which typically require more than 200 mJ per m^2 to generate them. Without the obstruction caused by stacking faults, the screw dislocations may easily cross-slip even under proportional loadings, since the many slip systems are able to well distribute the deformation in all possible directions in 3D. Slips of dislocations are wavy, changing their glide planes easily, even for uniaxial histories. Therefore, since cross-slip bands already happen naturally even under proportional loadings, NP histories do not cause any significant increase in strain hardening, and thus $\alpha_{NP} \cong 0$. Note, however, that α_{NP} depends not only on the material and on its microstructure, but also on the strain amplitudes involved in the load history [7–9]. In general, lower amplitudes are associated with lower α_{NP}.

When NP hardening is significant, NP multiaxial load histories can produce fatigue lives that are much lower than the ones induced by proportional histories with the same strain range $\Delta\varepsilon$, since this hardening increases the corresponding $\Delta\sigma$ range. Conversely, for materials with large additional hardening α_{NP} under stress-controlled loads, the fatigue lives are much longer under multiaxial NP loads than under proportional loads with the same stress range $\Delta\sigma$, due to the lower range $\Delta\varepsilon$ necessary to achieve this $\Delta\sigma$.

Note, however, that NP histories can decrease fatigue lives even in the absence of NP hardening. Most multiaxial fatigue damage models agree that damage depends both on an equivalent shear range $\Delta\varepsilon_{eq}$ (or equivalent stress range $\Delta\sigma_{eq}$ for high-cycle fatigue) and on the mean stress $\sigma_{\perp m}$ (or maximum $\sigma_{\perp max}$) perpendicular to the microcrack plane. An NP history with out-of-phase normal and shear strain ranges $\Delta\varepsilon$ and $\Delta\gamma$ can have a much higher $\Delta\varepsilon_{eq}$ than a proportional history with same $\Delta\varepsilon$ and $\Delta\gamma$, as predicted by most convex enclosure methods, as well as by the MOI method for estimating equivalent ranges [10], decreasing fatigue lives independently of the NP hardening effect, as verified in [8]. Additionally, NP hardening can also affect lives due to the $\sigma_{\perp max}$ term: NP hardening would cause a strain-controlled loading to increase its $\sigma_{\perp max}$ and thus further decrease the consequent fatigue lives. Conversely, as discussed before, for stress-controlled problems, NP hardening would cause a decrease in $\Delta\varepsilon_{eq}$ for a given $\Delta\sigma_{\perp}$, increasing fatigue lives. In summary, NP effects are not trivial to predict without proper modeling.

In general, NP strain hardening can be modeled using the same Ramberg–Osgood hardening exponent h_c from the cyclic uniaxial $\sigma - \varepsilon$ curve and using a new hardening coefficient $H_{NP} = H_c.(1 + \alpha_{NP}.F_{NP})$, where H_c is the cyclic strain-hardening coefficient calibrated under uniaxial conditions. Note that NP hardening can multiply H_c by a factor as high as 2, when both $\alpha_{NP} = 1$ and $F_{NP} = 1$.

To account for NP strain-hardening effects, it is necessary to not only measure α_{NP} but also correctly evaluate the NP factor F_{NP} associated with the multiaxial load history. The NP factor depends solely on the shape of the multiaxial load history path [11]. The largest NP factor, associated with $F_{NP} = 1$, happens for a 90° out-of-phase tension–torsion loading with same normal and effective shear amplitudes, as illustrated in Fig. 2(middle), which generates a circle in the von Mises $\sigma \times \tau \cdot \sqrt{3}$ stress diagram, see Fig. 3(middle), or in the $\varepsilon \times \gamma/\sqrt{3}$ strain diagram. Note that proportional multiaxial histories, which are associated with straight paths that cross the origin of the von Mises stress or strain diagram as shown in Fig. 3(left), do not cause NP hardening.

2 Nonproportionality factor estimates

The nonproportionality factor F_{NP} has been traditionally estimated from the aspect ratio of the convex enclosure that contains the multiaxial load history path. For instance, for zero-mean loads, F_{NP} is usually estimated from

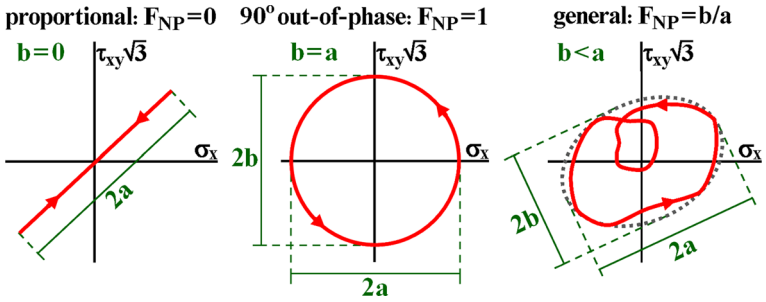

Fig. 3 Definition of the nonproportionality factor F_{NP} for proportional (*left*), 90° out-of-phase (*middle*), and general tension–torsion stress histories (*right*) [1]

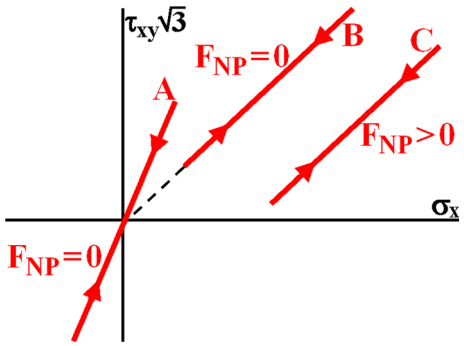

Fig. 4 In-phase tension–torsion stress paths that result in proportional histories for paths A and B and in an NP history for C

the aspect ratio b/a of an ellipse that encloses the stress path, where a and $b(b \leq a)$ are the ellipse semi-axes; see Fig. 3(right). Therefore, in-phase and 180° out-of-phase loadings (see Fig. 2), which always result in straight stress paths that cross the stress diagram origin, are also always proportional (thus having $F_{\mathrm{NP}} = 0$) under zero-mean loads; see Fig. 3(left). Sinusoidal 90° out-of-phase tension–torsion loadings with equal amplitudes for σ_x and $\tau_{xy}\sqrt{3}$ result in circular load paths, so they induce a $F_{\mathrm{NP}} = b/a = 1$, as expected; see Fig. 3(middle). Figure 3(right) shows the enclosing ellipse of a general periodic tension–torsion history, associated with an NP factor $0 \leq F_{\mathrm{NP}} \leq 1$.

Note that the general periodic tension–torsion load path exemplified in Fig. 3(right) is a combination of an outer and an inner loop that result in two different loading cycles per period, and therefore it can be classified as a variable amplitude loading (VAL) history. On the other hand, periodic paths consisting of just one cycle per period, such as the proportional and 90° out-of-phase NP examples from Fig. 3, are classified as constant amplitude loading (CAL) histories. Naturally, any nonperiodic and nonmonotonic path eventually results in a VAL history.

Note as well that in-phase or 180° out-of-phase loads can result in NP histories, as shown in Fig. 4 for the straight path C, which has a variable $\tau_{xy}(t)/\sigma_x(t)$ ratio (where t stands for time), and thus variable principal directions. But the straight path B, which is also in-phase with a nonzero-mean load, induces a proportional load history because it maintains a fixed $\tau_{xy}(t)/\sigma_x(t)$ ratio. The in-phase path A is also proportional, with a zero-mean load. Note that in-phase or out-of-phase biaxial histories induced by perpendicular normal loads (instead of tension–torsion) are always proportional, because they have constant principal stress directions (aligned with the load directions). So, multiaxial fatigue testing machines that use biaxial load frames with two perpendicular jacks cannot induce NP loads, and thus they are not as versatile as machines with tension–torsion frames.

However, as discussed in [10], convex enclosure estimates such as $F_{\mathrm{NP}} = b/a$ from the ellipse that encloses the load path can lead to poor predictions of F_{NP}. Moreover, the previous examples are simple, since they involve load histories with only two stress components. For a general six-dimensional (6D) stress history, F_{NP} estimates need to consider the path of all six stress components σ_x, σ_y, σ_z, τ_{xy}, τ_{xz}, and τ_{yz}.

Besides the methods based on convex enclosures, other empirical methods have been proposed to estimate F_{NP}, classified as phenomenological estimates [9]. Kanazawa et al. [12] estimated F_{NP} as a rotation factor, defined by the ratio between the maximum shear strain range and the shear strain range at 45° from the

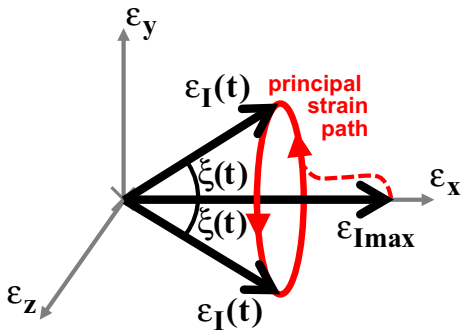

Fig. 5 Principal strain path that leads to a constant angle $\xi(t)$, exemplifying the inadequacy of Itoh's method for general 3D–6D multiaxial histories

maximum shear plane. This factor correctly tends to the limits $F_{\mathrm{NP}} = 0$ for proportional loadings and $F_{\mathrm{NP}} = 1$ for 90° out-of-phase strain histories. However, it fails to correctly compute F_{NP} for more complex-shaped load history paths, as experimentally verified in [9].

Itoh et al. [3] estimated F_{NP} using an integral definition along periodic strain paths:

$$F_{\mathrm{NP}} = \frac{\pi}{2T\varepsilon_{I\,\max}} \int_0^{\mathrm{T}} \varepsilon_I(t) \cdot |\sin \xi(t)| \cdot \mathrm{d}t \tag{1}$$

where $\varepsilon_I(t)$ is the absolute value of the maximum principal strain at each instant t, $\varepsilon_{I\,\max}$ is the maximum value of $\varepsilon_I(t)$ along the entire path, $\xi(t)$ is the angle between the principal directions associated with $\varepsilon_I(t)$ and $\varepsilon_{I\,\max}$, and T is the time period of the multiaxial load path. Similar to Kanazawa's idea, Itoh's method also tries to compute F_{NP} from changes in the principal strain direction, but Itoh's more general integral formulation allows the analysis of arbitrarily shaped multiaxial load history paths.

Albeit Itoh's original method from [3] provides reasonable F_{NP} predictions for simple 2D (e.g., tension–torsion) histories, it should not be applied to more general 3D to 6D histories, since it is based on a scalar measure, the angle $\xi(t)$, which is not enough to represent all possible variations of the principal strain direction in 3D. For instance, if the directions of $\varepsilon_I(t)$ along a load path describe a cone with symmetry axis in the direction of $\varepsilon_{I\,\max}$, as shown in Fig. 5, then $\xi(t)$ would be constant and equal to half the cone apex angle, regardless of the chosen path. However, constant amplitude or 90° out-of-phase cycles could result in the same $\xi(t)$ and $\varepsilon_I(t)$ histories, wrongfully calculating the same F_{NP} for both cases. Instead of using the scalar measure $\xi(t)$, the direction of $\varepsilon_I(t)$ would need to be defined by a vector of at least two elements to be able to distinguish between these load paths. As a result, even though Itoh's method has been formulated in a general 3D or 6D space [4], its estimates are not robust if the history is not 2D, as shown in the above counterexample.

Moreover, the definition of Itoh's method in the time domain is not appropriate to describe transient elastoplastic effects, which depend on the accumulated plastic strain, but not on time. Itoh's integral must assume a constant plastic strain rate to eliminate its time dependence. Finally, such approach is not appropriate even for 2D load paths when significant viscous or strain-rate effects are involved in the damage process, like when creep damage cannot be neglected for modeling purposes.

These issues were addressed in an improved version from Itoh et al. [4], where F_{NP} is calculated by a line integration along the 6D multiaxial loading path, using the loading amplitude and two angles related to the principal direction change. Using two angles instead of one, it is possible to overcome issues, for example, with the path from Fig. 5, correctly describing the 3D nature of the principal strain space. Moreover, by replacing time integration with path integration, time independence is guaranteed in the calculation, as expected in the absence of significant viscous effects.

To calculate F_{NP} for more general 6D load paths, Bishop [13] introduced a 6×6 inertia tensor termed the rectangular moment of inertia (RMOI) of the stress path, which can be expressed using Voigt-Mandel's [14] 6D stress representation $\vec{\sigma}$ by

$$I_\sigma \equiv (1/p_\sigma) \cdot \int (\vec{\sigma} - \vec{\sigma}_{\mathrm{m}}) \cdot (\vec{\sigma} - \vec{\sigma}_{\mathrm{m}})^{\mathrm{T}} \cdot |\mathrm{d}\vec{\sigma}| \tag{2}$$

where $|\mathrm{d}\vec{\sigma}|$ is the Euclidean norm of the 6D stress increment $\mathrm{d}\vec{\sigma}$, and the mean component $\vec{\sigma}_\mathrm{m}$ and path perimeter p_σ are also integrated along the 6D stress path, calculated from

$$\vec{\sigma}_\mathrm{m} \equiv (1/p_\sigma) \cdot \int \vec{\sigma} \cdot |\mathrm{d}\vec{\sigma}| \quad \text{and} \quad p_\sigma \equiv \int |\mathrm{d}\vec{\sigma}|. \tag{3}$$

The RMOI stress tensor measures the distribution of the stress path, relative to its mean, about the coordinate planes. Bishop proposed that F_NP could be estimated from the two largest eigenvectors $\lambda_{\sigma 1}$ and $\lambda_{\sigma 2}$ of $I_\sigma\,(\lambda_{\sigma 1} \geq \lambda_{\sigma 2})$ by

$$F_\mathrm{NP} = \sqrt{\lambda_{\sigma 2}/\lambda_{\sigma 1}}. \tag{4}$$

Note that the normalization factor $1/p_\sigma$ was not included in Bishop's original definition of I_σ, but it has been introduced here to simplify its comparison with the MOI method. Despite being more general than Itoh's method, Bishop's RMOI approach also has several limitations [11]:

(i) it is formulated in a stress space, instead of a plastic strain space, which would be more appropriate to describe a plasticity-induced effect such as NP hardening;
(ii) it uses a stress or strain formulation instead of a deviatoric one; hence, it implicitly assumes that the hydrostatic component might influence F_NP, which is not true for materials with pressure-insensitive yield behavior, like most metallic alloys in which the plastic behavior can be well described by von Mises; and
(iii) it calculates the moments of inertia relative to the mean component of the multiaxial load path, which is not able to describe the variation in principal directions, instead of relative to the origin of the stress or strain diagram.

Therefore, the F_NP estimate should be instead formulated in a plastic strain space, to be independent of the mean or hydrostatic components of stresses and strains. Thus, to eliminate any dependence of F_NP on hydrostatic components, the load history should be represented in a deviatoric stress or strain space, since they are not influenced by the hydrostatic components of the load path.

Nevertheless, several F_NP estimates are still based on diagrams involving a single normal component σ_x or ε_x and a single shear component τ_{xy} or γ_{xy}, which could lead to very large errors, instead of incorporating the contribution, for example, of σ_y or ε_y.

3 The moment of inertia (MOI) F_NP estimate

The moment of inertia (MOI) method was originally proposed by the authors in [10] to estimate path-equivalent stress and strain ranges and mean components. It was later extended in [11] to estimate F_NP in general 6D NP load histories, to compensate for the limitations in Itoh's, Bishop's, and other similar F_NP estimates. In this work, this general 6D formulation is reduced to a simpler computationally efficient 3D formulation assuming free-surface conditions, which can properly describe the conditions at the crack initiation location of most structural components.

The MOI method for F_NP has been originally defined in the 5D Euclidean deviatoric plastic strain space E_{5p}, which represents the plastic strain tensor using a 5D vector $\vec{e}'_\mathrm{pl}$ defined by:

$$\begin{cases} \vec{e}'_\mathrm{pl} \equiv [\, e_{1\mathrm{pl}}\ e_{2\mathrm{pl}}\ e_{3\mathrm{pl}}\ e_{4\mathrm{pl}}\ e_{5\mathrm{pl}}\,]^\mathrm{T}, \quad e_{1\mathrm{pl}} \equiv \varepsilon_{x\mathrm{pl}} - (\varepsilon_{y\mathrm{pl}} + \varepsilon_{z\mathrm{pl}})/2, \\ e_{2\mathrm{pl}} \equiv (\varepsilon_{y\mathrm{pl}} - \varepsilon_{z\mathrm{pl}})\frac{\sqrt{3}}{2}, \quad e_{3\mathrm{pl}} \equiv \gamma_{xy\mathrm{pl}}\frac{\sqrt{3}}{2}, \quad e_{4\mathrm{pl}} \equiv \gamma_{xz\mathrm{pl}}\frac{\sqrt{3}}{2}, \quad e_{5\mathrm{pl}} \equiv \gamma_{yz\mathrm{pl}}\frac{\sqrt{3}}{2}. \end{cases} \tag{5}$$

There are several motivations to prefer the 5D projection $\vec{e}'_\mathrm{pl}$ of the plastic strain space to calculate F_NP, over stress or strain spaces, as discussed in [11]. This deviatoric space is appropriate to define an integral equation to estimate F_NP, because, contrary to Bishop's method [13], it is independent of the hydrostatic components. Note that this $\vec{e}'_\mathrm{pl}$ vector is equal to the 5D representation of the plastic strains proposed by Tanaka [15] multiplied by 3/2:

$$\vec{e}'_\mathrm{pl} = \frac{3}{2} \cdot \underbrace{\left[\, e_{x_\mathrm{pl}}\ \ \frac{e_{x_\mathrm{pl}}+2e_{y_\mathrm{pl}}}{\sqrt{3}}\ \ \frac{\gamma_{xy_\mathrm{pl}}}{\sqrt{3}}\ \ \frac{\gamma_{xz_\mathrm{pl}}}{\sqrt{3}}\ \ \frac{\gamma_{yz_\mathrm{pl}}}{\sqrt{3}}\,\right]^\mathrm{T}}_{\text{Tanaka's 5D deviatoric space}} \tag{6}$$

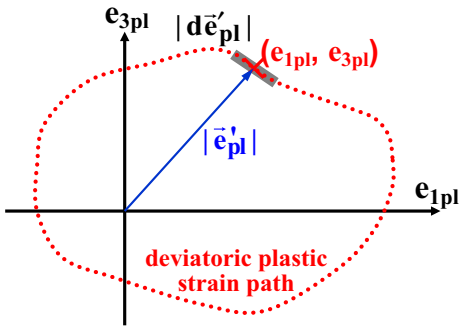

Fig. 6 Plastic strain path in the $e_{1\mathrm{pl}} \times e_{3\mathrm{pl}} = (3/2) \cdot (\varepsilon_{x\mathrm{pl}} \times \gamma_{xy\mathrm{pl}}/\sqrt{3})$ diagram for a 2D tension–torsion history

since the deviatoric identity $e_{x\mathrm{pl}} + e_{y\mathrm{pl}} + e_{z\mathrm{pl}} = 0$ implies that $e_{y\mathrm{pl}} - e_{z\mathrm{pl}} = e_{x\mathrm{pl}} + 2e_{y\mathrm{pl}}$.

Therefore, the presented 5D deviatoric formulation is highly recommended to solve 6D multiaxial stress-strain problems, due to its reduced computational cost without compromising accuracy, since the 5D results are exactly the same as the 6D ones in incremental plasticity calculations. Moreover, the 5D formulation separates deviatoric and hydrostatic components, guaranteeing that plastic incompressibility is not violated even after several discrete integration steps in an incremental plasticity formulation.

To calculate the directions suffering the largest plastic strain magnitudes, the plastic strain path in its E_{5p} space is imagined as a homogeneous wire with unit mass; see Fig. 6. The moments of inertia of such unit mass wire with respect to the deviatoric space origin are related to how much the plastic path stretches in each considered direction. Therefore, such moments of inertia could be correlated with how much accumulated plastic straining there is in such a direction.

The MOI method to estimate F_{NP} is reviewed next in its generalized version for a 6D multiaxial history containing all three normal and three shear components. First, the plastic strain path in all six directions must be obtained, either from incremental plasticity calculations or from measurements of both stress and total strain histories. The plastic strain path is then represented in the five-dimensional E_{5p} space.

The MOI method follows a direct analogy with the moment of inertia tensor of a solid, as studied in classic dynamics books. The plastic strain path is imagined as a homogeneous wire with unit mass, whose moments of inertia define how much the path stretches along each individual direction. However, dynamics books usually adopt the axial MOI (AMOI), the moment of inertia about a given axis, which is a measure of how much the solid (the wire in our case) stretches in every *other* direction perpendicular to this axis. To calculate how much the plastic strain path stretches along each individual direction, the 5×5 rectangular MOI (RMOI) matrix $I_{\mathrm{r}}^{\mathrm{O}}$ of the plastic strain path $\vec{e}'_{\mathrm{pl}}$ with respect to the diagram origin O is used instead. The RMOI gives the moments of inertia about the planes (or hyperplanes) perpendicular to each considered direction, i.e., the distribution of the stress path about the coordinate planes:

$$I_{\mathrm{r}}^{\mathrm{O}} = \frac{1}{p} \cdot \int \vec{e}'_{\mathrm{pl}} \cdot \vec{e}'^{\mathrm{T}}_{\mathrm{pl}} \cdot \mathrm{d}p = \frac{1}{p} \cdot \int \begin{bmatrix} e_{1\mathrm{pl}}^2 & e_{1\mathrm{pl}} \cdot e_{2\mathrm{pl}} & e_{1\mathrm{pl}} \cdot e_{3\mathrm{pl}} & e_{1\mathrm{pl}} \cdot e_{4\mathrm{pl}} & e_{1\mathrm{pl}} \cdot e_{5\mathrm{pl}} \\ e_{2\mathrm{pl}} \cdot e_{1\mathrm{pl}} & e_{2\mathrm{pl}}^2 & e_{2\mathrm{pl}} \cdot e_{3\mathrm{pl}} & e_{2\mathrm{pl}} \cdot e_{4\mathrm{pl}} & e_{2\mathrm{pl}} \cdot e_{5\mathrm{pl}} \\ e_{3\mathrm{pl}} \cdot e_{1\mathrm{pl}} & e_{3\mathrm{pl}} \cdot e_{2\mathrm{pl}} & e_{3\mathrm{pl}}^2 & e_{3\mathrm{pl}} \cdot e_{4\mathrm{pl}} & e_{3\mathrm{pl}} \cdot e_{5\mathrm{pl}} \\ e_{4\mathrm{pl}} \cdot e_{1\mathrm{pl}} & e_{4\mathrm{pl}} \cdot e_{2\mathrm{pl}} & e_{4\mathrm{pl}} \cdot e_{3\mathrm{pl}} & e_{4\mathrm{pl}}^2 & e_{4\mathrm{pl}} \cdot e_{5\mathrm{pl}} \\ e_{5\mathrm{pl}} \cdot e_{1\mathrm{pl}} & e_{5\mathrm{pl}} \cdot e_{2\mathrm{pl}} & e_{5\mathrm{pl}} \cdot e_{3\mathrm{pl}} & e_{5\mathrm{pl}} \cdot e_{4\mathrm{pl}} & e_{5\mathrm{pl}}^2 \end{bmatrix} \cdot \mathrm{d}p \quad (7)$$

where $\mathrm{d}p$ is the equivalent plastic strain increment and p is the accumulated plastic strain, which is proportional to the perimeter of the plastic strain path in the E_{5p} space, since

$$\mathrm{d}p \equiv (2/3) \cdot |\mathrm{d}\vec{e}'_{\mathrm{pl}}| \quad \text{and} \quad p \equiv \int \mathrm{d}p = (2/3) \cdot \int |\mathrm{d}\vec{e}'_{\mathrm{pl}}| = (2/3) \cdot (\text{perimeter}). \quad (8)$$

Tanaka [15] has shown that F_{NP} has a transient behavior. For periodic variable amplitude loading (VAL) with several cycles per period or for nonperiodic histories, the NP hardening evolution requires differential equations and a polarization tensor to be computed. However, if the loading is periodic and each period consists of one or just a few VAL cycles, then F_{NP} converges to a constant steady-state value after the NP hardening transient. In this case, the MOI method performs the integration from Eq. (7) along one full period to find $I_{\mathrm{r}}^{\mathrm{O}}$.

The eigenvalues $\lambda_{p1}, \lambda_{p2}, \ldots, \lambda_{p5}$ of I_r^O (ordered such that $\lambda_{p1} \geq \lambda_{p2} \geq \cdots \geq \lambda_{p5}$) are the scalar RMOI values along the principal directions of the path, which are used to describe the nonproportionality of the load history. They are a measure of the accumulated plastic strains along each principal direction of the stress/strain state defined by the associated unit eigenvectors $\vec{v}_{p1}, \vec{v}_{p2}, \ldots, \vec{v}_{p5}$. These unit eigenvectors constitute an orthonormal system, being mutually perpendicular due to the fact that I_r^O is symmetric. These eigenvectors of the RMOI tensor represent the principal axes of the plastic strain path, which may be used as a "reference frame" to define the out-of-phase extent of a load history by the combination of the associated eigenvalues. Following this reasoning, the MOI method's F_{NP} estimate is defined as the square root of the ratio between the two largest eigenvalues of the RMOI tensor I_r^O, i.e.,

$$F_{NP} = \sqrt{\lambda_{p2}/\lambda_{p1}}. \tag{9}$$

For instance, in a proportional loading, the plastic strain path describes a straight segment that crosses the diagram origin, analogous to a straight wire, which has only one nonzero principal RMOI $\lambda_{p1} > 0$, while $\lambda_{p2} = \lambda_{p3} = \lambda_{p4} = \lambda_{p5} = 0$, and thus $F_{NP} = 0$, as expected. On the other hand, a circular history with zero-mean stress has two equal and nonzero principal RMOI $\lambda_{p1} = \lambda_{p2}$, giving $F_{NP} = 1$, as expected for such a 90° out-of-phase loading.

A 6D space could be used in Eq. (7) instead of the adopted 5D deviatoric subspace, but in this case the plastic strain component along the hydrostatic direction would always be zero for pressure-insensitive materials, those whose yield function does not depend on the hydrostatic component, such as von Mises, and thus whose hydrostatic strains are always elastic. Therefore, a sixth eigenvalue λ_{p6} equal to zero would always be found in 6D, along a corresponding sixth eigenvector $\vec{v}_{p6}$ in the hydrostatic direction. Since Eq. (9) is independent of such a λ_{p6}, the MOI method would provide identical F_{NP} estimates in both 6D and 5D. Thus, the computationally efficient 5D formulation from Eq. (5) is preferred in the I_r^O definition.

However, Tanaka's 5D deviatoric space adopted in this work, as seen in Eqs. (5–6), has an issue with biaxial loadings without plastic shear strain components, wrongfully predicting $F_{NP} > 0$. Such biaxial loadings, usually tested in cruciform specimens, do not cause NP hardening because the principal directions do not change, while the maximum absolute principal stress direction only changes by a factor of 90°. Indeed, e.g., pure cyclic torsion does not cause NP hardening, even though such maximum absolute stress keeps changing by 90° at every reversal. This issue with Tanaka's NP hardening model has not been noticed in the literature because the model has been verified for tension–torsion histories, but never checked against biaxial loadings without shear.

Nevertheless, it is easy to detect such a biaxial case. For Tanaka's model, the two largest eigenvalues of its polarization tensor would be associated with eigenvalues almost entirely contained in the $e_{1pl} - e_{2pl}$ plane, which accounts for normal plastic strains, without significant components in the remaining e_{3pl}, e_{4pl}, and e_{5pl} shear directions. The same reasoning can be applied to the RMOI tensor from Eq. (7), where Eq. (9) would only be applicable if the eigenvectors $\vec{v}_{p1}$ and $\vec{v}_{p2}$ (associated with the highest eigenvalues λ_{p1} and λ_{p2}) are not contained in the $e_{1pl} - e_{2pl}$ plane, or nearly parallel to it. In this case, one *ad hoc* approach would be to replace λ_{p2} with λ_{p3} in Eq. (9), which would be associated with an eigenvector $\vec{v}_{p3}$ in the shear subspace $e_{3pl} - e_{4pl} - e_{5pl}$. In other words, if the two main plastic straining directions $\vec{v}_{p1}$ and $\vec{v}_{p2}$ are essentially normal, F_{NP} should be evaluated from the ratio between the highest shear eigenvalue λ_{p3} and the highest normal eigenvalue λ_{p1} to account for their relative influence changing the principal directions.

A more general approach could somehow combine the first two rows and first two columns in Eq. (7) to merge both normal terms and thus reduce the RMOI to a 4×4 matrix, whose eigenvalues could be used in Eq. (9). But experimental measurements on a 3D multiaxial test machine, capable of independently applying two normal and one shear stress histories, would be required to properly evaluate this proposal.

4 MOI F_{NP} estimate under free-surface conditions

In this paper, the original 5D MOI formulation to estimate F_{NP} is reduced to a computationally efficient 3D formulation that is suitable to describe the multiaxial behavior of critical points under free-surface conditions, the most common case in practical applications. Assuming the free surface normal to the z direction, the shear strain components γ_{xz} and γ_{yz} are zero, and thus their plastic components are $\gamma_{xzpl} = \gamma_{yzpl} = 0$. It follows that the five-dimensional E_{5p} space can be reduced to a three-dimensional E_{3p} plastic strain space, defined using the 3D vector $\vec{e}''_{pl}$ given by

$$\begin{cases} \vec{e}''_{\mathrm{pl}} \equiv [\, e_{1\mathrm{pl}} \; e_{2\mathrm{pl}} \; e_{3\mathrm{pl}} \,]^{\mathrm{T}}, \, e_{1\mathrm{pl}} \equiv \varepsilon_{x\mathrm{pl}} - (\varepsilon_{y\mathrm{pl}} + \varepsilon_{z\mathrm{pl}})/2, \\ e_{2\mathrm{pl}} \equiv (\varepsilon_{y\mathrm{pl}} - \varepsilon_{z\mathrm{pl}})\frac{\sqrt{3}}{2}, \, e_{3\mathrm{pl}} \equiv \gamma_{xy\mathrm{pl}}\frac{\sqrt{3}}{2}. \end{cases} \tag{10}$$

The free-surface plastic strain $\varepsilon_{z\mathrm{pl}}$ is in general not equal to zero, due to plastic Poisson effects and the plastic incompressibility condition $\varepsilon_{x\mathrm{pl}} + \varepsilon_{y\mathrm{pl}} + \varepsilon_{z\mathrm{pl}} = 0$. This linear dependence condition is automatically satisfied in the above 3D formulation, and it is also the reason why four plastic strain components ($\varepsilon_{x\mathrm{pl}}$, $\varepsilon_{y\mathrm{pl}}$, $\varepsilon_{z\mathrm{pl}}$, and $\gamma_{xy\mathrm{pl}}$) can be represented in a 3D (instead of 4D) formulation.

It is not uncommon to find incremental plasticity formulations using 4, 6, or even 9 (redundant) components to describe plastic straining under free-surface conditions, which not only decreases computational efficiency, but also might allow discrete plastic strain increments $\Delta\varepsilon_{x\mathrm{pl}} + \Delta\varepsilon_{y\mathrm{pl}} + \Delta\varepsilon_{z\mathrm{pl}} \neq 0$ due to the accumulation of numerical errors in implicit numerical integration schemes. The 3D formulation proposed here, on the other hand, could be used in plasticity calculations under free-surface conditions without any problems involving violation of plastic incompressibility. Moreover, this 3D formulation in E_{3p} significantly simplifies the use of the MOI method to estimate F_{NP}. After obtaining the successive values of the 3D plastic strain vector $\vec{e}''_{\mathrm{pl}}$ along the history, this path is integrated to obtain a 3×3 version of the RMOI tensor $I_{\mathrm{r}}^{\mathrm{O}}$, given by

$$I_{\mathrm{r}}^{\mathrm{O}} = \frac{1}{p} \cdot \int \vec{e}''_{\mathrm{pl}} \cdot \vec{e}''^{\mathrm{T}}_{\mathrm{pl}} \cdot \mathrm{d}p = \frac{1}{p} \cdot \int \begin{bmatrix} e_{1\mathrm{pl}}^2 & e_{1\mathrm{pl}} \cdot e_{2\mathrm{pl}} & e_{1\mathrm{pl}} \cdot e_{3\mathrm{pl}} \\ e_{2\mathrm{pl}} \cdot e_{1\mathrm{pl}} & e_{2\mathrm{pl}}^2 & e_{2\mathrm{pl}} \cdot e_{3\mathrm{pl}} \\ e_{3\mathrm{pl}} \cdot e_{1\mathrm{pl}} & e_{3\mathrm{pl}} \cdot e_{2\mathrm{pl}} & e_{3\mathrm{pl}}^2 \end{bmatrix} \cdot \mathrm{d}p \tag{11}$$

where $\mathrm{d}p \equiv (2/3) \cdot |\mathrm{d}\vec{e}''_{\mathrm{pl}}|$ and $p \equiv \int \mathrm{d}p = (2/3) \cdot \int |\mathrm{d}\vec{e}''_{\mathrm{pl}}| = (2/3) \cdot (\text{perimeter})$. The F_{NP} estimate is then obtained from Eq. (9) and the two largest eigenvalues from $I_{\mathrm{r}}^{\mathrm{O}}$. As mentioned before, be careful with biaxial normal histories without significant shear components, where the two largest eigenvalues λ_{p1} and λ_{p2} would be associated with normal plastic strains. Without significant shear (i.e., $\lambda_{p3} \cong 0$ if in this case), such biaxial normal plastic strains would not cause variation of the principal directions (except for 90° changes of their maximum absolute direction), and thus F_{NP} should tend to zero. If the eigenvalue λ_{p3} is mainly associated with the shear component and $\lambda_{p3} > 0$, then it should be used instead in the numerator of Eq. (9).

For a tension–torsion history in an un-notched specimen, it is possible to further reduce the plastic strain formulation to a 2D space. Under histories of tensile σ_x and shear τ_{xy}, a symmetry argument in y and z shows that $e_{2\mathrm{pl}} \equiv (\varepsilon_{y\mathrm{pl}} - \varepsilon_{z\mathrm{pl}})\sqrt{3}/2 = 0$. Therefore, an even simpler two-dimensional E_{2p} plastic strain space can be proposed, defined using the 2D vector $\vec{e}'''_{\mathrm{pl}}$ given by

$$\vec{e}'''_{\mathrm{pl}} \equiv [\, e_{1\mathrm{pl}} \; e_{3\mathrm{pl}} \,]^{\mathrm{T}}, \, e_{1\mathrm{pl}} \equiv \varepsilon_{x\mathrm{pl}} - (\varepsilon_{y\mathrm{pl}} + \varepsilon_{z\mathrm{pl}})/2, \, e_{3\mathrm{pl}} \equiv \gamma_{xy\mathrm{pl}}\sqrt{3}/2. \tag{12}$$

Analogous to the 3D case, it is possible to define a 2×2 version of $I_{\mathrm{r}}^{\mathrm{O}}$, given by

$$I_{\mathrm{r}}^{\mathrm{O}} = \frac{1}{p} \cdot \int \vec{e}'''_{\mathrm{pl}} \cdot \vec{e}'''^{\mathrm{T}}_{\mathrm{pl}} \cdot \mathrm{d}p = \frac{1}{p} \cdot \int \begin{bmatrix} e_{1\mathrm{pl}}^2 & e_{1\mathrm{pl}} \cdot e_{3\mathrm{pl}} \\ e_{3\mathrm{pl}} \cdot e_{1\mathrm{pl}} & e_{3\mathrm{pl}}^2 \end{bmatrix} \cdot \mathrm{d}p \tag{13}$$

where $\mathrm{d}p \equiv (2/3) \cdot |\mathrm{d}\vec{e}'''_{\mathrm{pl}}|$ and $p \equiv \int \mathrm{d}p = (2/3) \cdot \int |\mathrm{d}\vec{e}'''_{\mathrm{pl}}| = (2/3) \cdot (\text{perimeter})$. Note that both eigenvalues from $I_{\mathrm{r}}^{\mathrm{O}}$ are then used in Eq. (9) to estimate F_{NP}.

The RMOI tensor $I_{\mathrm{r}}^{\mathrm{O}}$ can also be numerically calculated for polygonal load history paths used in computational implementations with discrete finite increments. If $\vec{e}''_{\mathrm{pl}}$ is the 3D plastic strain vector in the E_{3p} space at each calculation step and if $\Delta\vec{e}''_{\mathrm{pl}}$ is the associated finite plastic strain increment, then the RMOI integral from Eq. (11) can be estimated from a summation based on Simpson's rule,

$$I_{\mathrm{r}}^{\mathrm{O}} \cong \frac{1}{6p} \cdot \sum \left[\vec{e}''_{\mathrm{pl}} \vec{e}''^{\mathrm{T}}_{\mathrm{pl}} + (\vec{e}''_{\mathrm{pl}} + \Delta\vec{e}''_{\mathrm{pl}})(\vec{e}''_{\mathrm{pl}} + \Delta\vec{e}''_{\mathrm{pl}})^{\mathrm{T}} + 4 \cdot (\vec{e}''_{\mathrm{pl}} + \Delta\vec{e}''_{\mathrm{pl}}/2)(\vec{e}''_{\mathrm{pl}} + \Delta\vec{e}''_{\mathrm{pl}}/2)^{\mathrm{T}} \right] \cdot \Delta p, \tag{14}$$

where the discrete increment Δp and the accumulated plastic strain p are given by

$$\Delta p \equiv (2/3) \cdot |\Delta\vec{e}''_{\mathrm{pl}}| \quad \text{and} \quad p = \sum \Delta p. \tag{15}$$

The above discrete implementation can also be applied to the 2D tension–torsion formulation of plastic strains, replacing $\vec{e}''_{\mathrm{pl}}$ and $\Delta\vec{e}''_{\mathrm{pl}}$ by $\vec{e}'''_{\mathrm{pl}}$ and $\Delta\vec{e}'''_{\mathrm{pl}}$ in Eqs. (14–15).

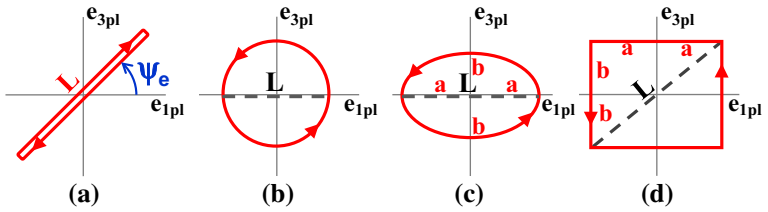

Fig. 7 Calculation of F_{NP} from the 2D version of the MOI method for proportional, circular, elliptical, and rectangular plastic strain paths in the $e_{1\mathrm{pl}} \times e_{3\mathrm{pl}}$ diagram. Note that for a tension–torsion history, this diagram is proportional to $\varepsilon_{x\mathrm{pl}} \times \gamma_{xy\mathrm{pl}}/\sqrt{3}$

The proposed approach is evaluated by F_{NP} estimates for some simple tension–torsion plastic strain histories, using the proposed 2D MOI formulation. A proportional elastoplastic tension–torsion history always results in a plastic strain path described by a straight segment going through the origin O of the $e_{1\mathrm{pl}} \times e_{3\mathrm{pl}}$ diagram; see Fig. 7a. If this straight segment has length L (thus, the plastic strain path has perimeter $2L$) and makes a constant angle ψ_e with the $e_{1\mathrm{pl}}$ axis, then the accumulated plastic strain p and the associated RMOI tensor for a full cycle become

$$p = \frac{2}{3} \cdot (2L) = \frac{4L}{3} \quad \text{and} \quad I_{\mathrm{r}}^{\mathrm{O}} = \frac{1}{12} \begin{bmatrix} L^2 \cos^2 \psi_e & L^2 \sin \psi_e \cos \psi_e \\ L^2 \sin \psi_e \cos \psi_e & L^2 \sin^2 \psi_e \end{bmatrix} \tag{16}$$

whose eigenvalues $\lambda_{p1} = L^2/12$ and $\lambda_{p2} = 0$ result in $F_{\mathrm{NP}} = \sqrt{\lambda_{p2}/\lambda_{p1}} = 0$, as expected.

Consider now the 90° out-of-phase 2D tension–torsion history from Fig. 7b. From symmetry considerations, a tension–torsion load history that describes a circular path in the total strain diagram $e_1 \times e_3$ should also describe a circle in the $e_{1\mathrm{pl}} \times e_{3\mathrm{pl}}$ plastic strain diagram. If L is the diameter of such a circle, it follows for a full cycle that

$$p = \frac{2}{3} \cdot (\pi L) = \frac{2\pi L}{3} \quad \text{and} \quad I_{\mathrm{r}}^{\mathrm{O}} = \begin{bmatrix} L^2/8 & 0 \\ 0 & L^2/8 \end{bmatrix} \tag{17}$$

whose equal eigenvalues $\lambda_{p1} = \lambda_{p2} = L^2/8$ result in $F_{\mathrm{NP}} = \sqrt{\lambda_{p2}/\lambda_{p1}} = 1$, as expected.

The elliptical path from Fig. 7c does not have an analytical expression for $I_{\mathrm{r}}^{\mathrm{O}}$; however, a numerical integration results in $F_{\mathrm{NP}} = \sqrt{\lambda_{p2}/\lambda_{p1}} \cong b/a$ with a 6.4 % RMS error for ratios $0 < b/a \leq 1$. This F_{NP} estimate is coherent with the convex enclosure estimate from Fig. 3.

However, convex enclosure methods have a major limitation: They cannot tell apart convex from nonconvex paths that share the same enclosure. The MOI method, on the other hand, considers the shape of the entire multiaxial load path in the integral calculation, better describing the nonproportionality of the load history.

Finally, consider the plastic strain history from Fig. 7d, which describes a rectangle centered at the origin of the $e_{1\mathrm{pl}} \times e_{3\mathrm{pl}}$ diagram with sides $2a$ and $2b (a \geq b)$. From Eq. (15), the accumulated plastic strain for each full cycle is $p = 2/3 \cdot (4a + 4b)$, where $(4a + 4b)$is the rectangle perimeter. The RMOI $I_{\mathrm{r}}^{\mathrm{O}}$ is the sum of the tensors $I_{\mathrm{r}}^{\mathrm{Oh}}$ and $I_{\mathrm{r}}^{\mathrm{Ov}}$, associated, respectively, with the two horizontal and two vertical path segments. Each of the two horizontal path segments has a constant $e_{3\mathrm{pl}}^2 = b^2$ and $e_{1\mathrm{pl}}$ varying between $-a$ and a with an equivalent plastic strain variation $\Delta p_h = (2/3) \cdot (2a) = 4a/3$, while each of the two vertical segments has a constant $e_{1\mathrm{pl}}^2 = a^2$ and $e_{3\mathrm{pl}}$ varying between $-b$ and b with $\Delta p_v = (2/3) \cdot (2b) = 4b/3$. It follows that

$$\begin{aligned} I_{\mathrm{r}}^{\mathrm{O}} &= I_{\mathrm{r}}^{\mathrm{Oh}} + I_{\mathrm{r}}^{\mathrm{Ov}} = \frac{2 \cdot \Delta\rho_{\mathrm{h}}}{p} \cdot \begin{bmatrix} a^2/3 & 0 \\ 0 & b^2 \end{bmatrix} + \frac{2 \cdot \Delta\rho_{\mathrm{v}}}{p} \cdot \begin{bmatrix} a^2 & 0 \\ 0 & b^2/3 \end{bmatrix} \\ &= \frac{1}{a+b} \cdot \begin{bmatrix} ba^2 + a^3/3 & 0 \\ 0 & ab^2 + b^3/3 \end{bmatrix}, \end{aligned} \tag{18}$$

and, since $b \leq a$, the eigenvalues of $I_{\mathrm{r}}^{\mathrm{O}}$ result in the estimate

$$F_{\mathrm{NP}} = \sqrt{\frac{\lambda_{p2}}{\lambda_{p1}}} = \sqrt{\frac{ab^2 + b^3/3}{ba^2 + a^3/3}} = \frac{b}{a} \cdot \sqrt{\frac{3 + b/a}{1 + 3 \cdot b/a}}. \tag{19}$$

The extreme values of the above estimate are coherent with experimental data, predicting $F_{NP} = 0$ for a proportional loading with $b/a = 0$, and $F_{NP} = 1$ for a square loading path with $b/a = 1$, whose convex enclosure would be a circle and thus confirm the estimate $F_{NP} = 1$.

Finally, even though both MOI and Bishop's methods estimate F_{NP} using somewhat similar integrals and eigenvalue expressions, their results are quite different, since the former uses the principal RMOI of *deviatoric plastic strain* paths with respect to the *origin* O, while the latter uses the principal RMOI of the *stress* paths with respect to their *mean* component.

5 Experimental evaluation of F_{NP} predictions

There are no commercial testing machines capable of independently applying six stress components to a test specimen; therefore, it would not be easy to experimentally evaluate the effectiveness of the 6D F_{NP} predictions for general multiaxial loading conditions. Nevertheless, the evaluation of the 3D and 2D-based predictions of F_{NP} can be performed using tension–torsion experiments and simulations. The evolution of the von Mises stress from tension–torsion experiments can be compared with the corresponding von Mises value of an incremental plasticity simulation without considering NP hardening. The ratio between these values should describe the evolution of the $(1 + \alpha_{NP} F_{NP})$ term. Once the material parameter α_{NP} is calibrated, the evolution F_{NP} can be "experimentally measured" in an iterative process involving numerical simulations with different F_{NP} until finding the one that minimizes the root-mean-square error between the predicted and experimental stress paths (for a given strain history).

Figure 8 exemplifies this routine, for 90° out-of-phase tension–torsion experiments. For a given strain history describing circular paths in the $\varepsilon_x \times \gamma_{xy}/\sqrt{3}$ diagram, the experimentally measured resulting stresses are plotted in a $\sigma_x \times \tau_{xy}\sqrt{3}$ diagram, from which the evolution of the von Mises stress $\sqrt{\sigma_x^2 + 3\tau_{xy}^2}$ with the accumulated plastic strain p is obtained. An incremental plasticity simulation is then performed on the given strain history, calculating the stress evolution *without* considering NP hardening. Then, the ratio between the von Mises stresses between the experiments and simulations estimates the evolution of the $(1+\alpha_{NP} F_{NP})$ term, used to calibrate the evolution of F_{NP} for a given (previously calibrated) α_{NP}. The obtained F_{NP} is used again in a new incremental plasticity simulation to check whether the calculated path agrees with the experimental path within a desired calibration tolerance. If they still differ, then the ratio between the von Mises stresses from the experiments and simulations is once again calculated to fine-tune the value of F_{NP}. This process continues until F_{NP} is "calibrated" within a desired tolerance.

Experimental tension–torsion measurements from Itoh et al. [3] and Kida et al. [16] are used to evaluate Bishop's estimate and the presented 2D version of the MOI method to calculate F_{NP}. The experiments were

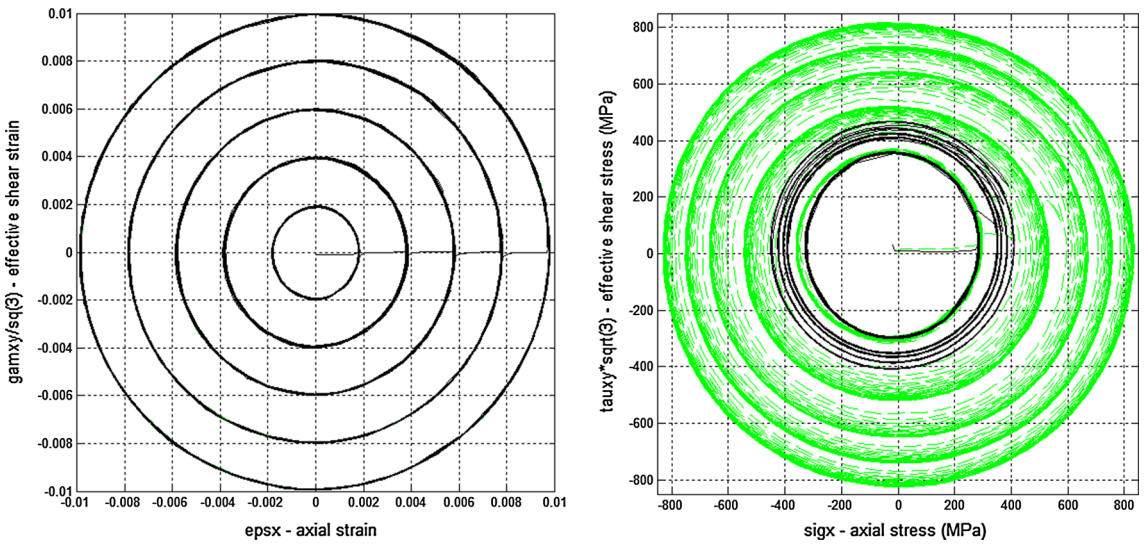

Fig. 8 *Left* Applied 90° out-of-phase tension–torsion strains in the $\varepsilon_x \times \gamma_{xy}/\sqrt{3}$ diagram; *right* resulting stresses in the $\sigma_x \times \tau_{xy}\sqrt{3}$ diagram obtained from 316L-steel simulations neglecting NP hardening (*solid line*) and from experiments (*dashed curve*)

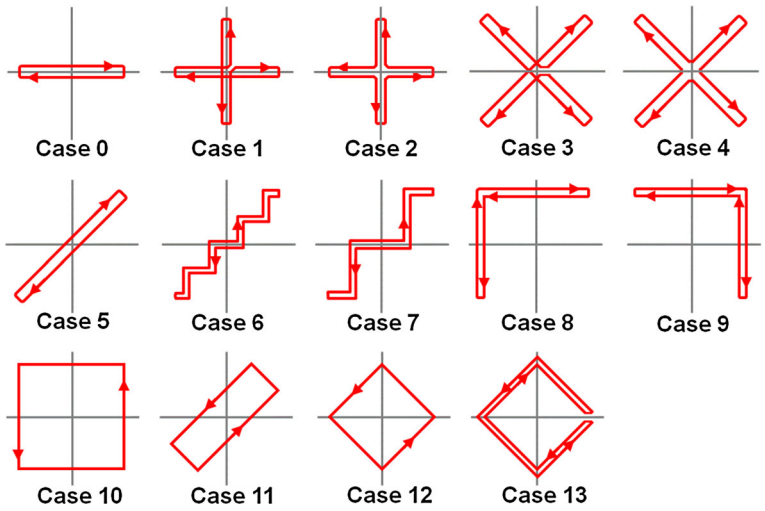

Fig. 9 Strain paths $\varepsilon_x \times \gamma_{xy}/\sqrt{3}$ used in the experimental validation of the F_{NP} predictions

performed in a 304 stainless steel with Young's modulus $E = 200\,\text{GPa}$, shear modulus $G = 82\,\text{MPa}$, uniaxial cyclic hardening coefficient $H_c = 670\,\text{MPa}$ and exponent $h_c = 0.125$, and additional hardening coefficient $\alpha_{\text{NP}} = 0.9$. Fourteen periodic histories are studied, represented by the strain paths $\varepsilon \times \gamma_{xy}/\sqrt{3}$ shown in Fig. 9 for Cases 0 through 13. The normal strain range $\Delta\varepsilon$ of all studied experimental data is fixed near 0.8 %, to avoid issues with the strain amplitude dependence of α_{NP}.

The associated plastic strain history in each case is evaluated from incremental plasticity calculations using Jiang–Sehitoglu's nonlinear kinematic model [17]. The material parameters are calibrated from uniaxial data using the procedure described in [18], neglecting transient ratcheting effects. NP hardening is considered in the model by continuously changing the generalized plastic modulus coefficients $c^{(i)}$ [17] from each hardening surface i, by the equation

$$c^{(i)}(p) = c^{(i)} \cdot [H_{\text{NP}}(p)/H_c]^{1/h_c},\ H_{\text{NP}}(p) = \underbrace{H_c \cdot [1 + \alpha_{\text{NP}} \cdot F_{\text{NP}}(p)]}_{\text{NP evolution}} \tag{20}$$

where H_c and h_c are Ramberg–Osgood's uniaxial cyclic hardening coefficient and exponent, $H_{\text{NP}}(p)$ is the current Ramberg–Osgood coefficient considering NP hardening, and p is the accumulated plastic strain.

For each strain-controlled loading Case 0 through 13, the incremental plasticity code is iteratively executed for several candidate values of F_{NP}, until the root-mean-square (RMS) error between the calculated and the measured strain paths in the $\sigma \times \tau\sqrt{3}$ diagram is minimized. The value of F_{NP} that minimizes the RMS error for each of the 14 paths is assumed to be the experimentally measured NP factor, which is compared in Fig. 10 with the predictions from Bishop and the 2D version of the MOI method. As shown in the figure, the MOI method predicts better values for F_{NP} than Bishop's method, which overestimates roughly by a factor of 2 or more the NP factors of load histories with low values $0 < F_{\text{NP}} < 0.5$ such as Cases 6, 7, and 11, confirming the calculations from [11] that used the original 5D MOI formulation. Moreover, Itoh's method underestimates F_{NP} for cross- and star-shaped load histories, as shown in Cases 1–4 in Fig. 10.

6 Conclusions

The MOI method is able to predict the nonproportionality factor F_{NP} of periodic multiaxial histories, evaluating the out-of-phase extent of a loading history based on the eigenvalues of the rectangular moment of inertia of the plastic strain path. This measure of F_{NP} is independent of the particular choice of the coordinate system, being invariant under coordinate transformations. Contrary to convex enclosure methods, the MOI method accounts for the contribution of every single segment of the load path, dealing with arbitrarily shaped histories without losing information about their shape. The MOI calculation is applicable to both constant and variable amplitude loading, as long as it is periodic and the steady-state value of F_{NP} does not vary significantly along each period (which is usually the case in most practical periodic load histories).

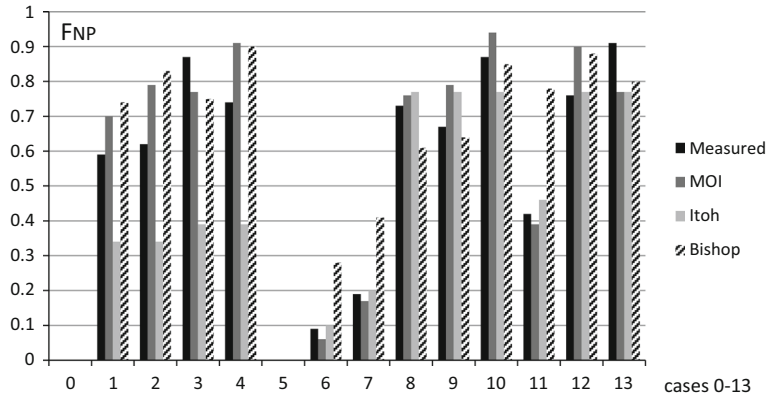

Fig. 10 Experimentally measured and predicted F_{NP} from the MOI, Itoh's and Bishop's methods for Cases 0 through 13, for a 304 stainless steel at strain range levels near 0.8 %. Note that the proportional Cases 0 and 5 result in zero NP factors

Under free-surface conditions, the proposed 3D and 2D versions of the MOI method exactly reproduce the 5D MOI predictions, with a lower computational cost. The 3D formulation for free surfaces is simpler and more computationally efficient than the 5D and 6D formulations, also with the advantage of guaranteeing plastic strain incompressibility, a major numerical issue in many 6D simulators. To quantitatively evaluate the efficiency of the 3D formulation, the relative computational times of all incremental plasticity simulations from this paper were evaluated, all of them including Tanaka's NP and Jiang's nonlinear kinematic hardening models. Compared to the computational times using a 6D formulation, on average the 5D formulation only took 47 % of the total time, the 3D took 40 %, and a further reduced 2D model (useful, for example, for tension–torsion histories) took only 33 %. Experimental results demonstrated the effectiveness of the proposed approach.

Acknowledgments The authors would like to acknowledge Prof. Darrell F. Socie for providing the experimental data used in the analyses. This work was supported in part by the National Natural Science Foundation of P.R. China under Grant No. 11302150. CNPq, Brazil, provided research fellowships for Profs. Marco A. Meggiolaro and Jaime T. P. Castro.

References

1. Socie, D.F., Marquis, G.B.: Multiaxial Fatigue. Society of Automotive Engineers, Inc., Warrendale (2000)
2. Itoh, T., Yang, T.: Material dependence of multiaxial low cycle fatigue lives under non-proportional loading. Int. J. Fatigue **33**, 1025–1031 (2011)
3. Itoh, T., Sakane, M., Ohnami, M., Socie, D.F.: Nonproportional low cycle fatigue criterion for type 304 stainless steel. ASME J. Eng. Mater. Technol. **117**, 285–292 (1995)
4. Itoh, T., Sakane, M.: Evaluation of multiaxial low cycle fatigue life under non-proportional loading. In: Tenth International Conference on Multiaxial Fatigue & Fracture (ICMFF10), Kyoto, Japan (2013)
5. Doquet, V., Clavel, M.: Stacking-fault energy and cyclic hardening of FCC solid solutions under multiaxial non-proportional loadings. In: Pineau, A., Cailletaud, G., Lindley, T.C. (eds.) Multiaxial Fatigue and Design, ESIS 21, pp. 43–60. Mechanical Engineering Publication, London (1996)
6. Taleb, L., Hauet, A.: Multiscale experimental investigations about the cyclic behavior of the 304L SS. Int. J. Plast. **25**, 1359–1385 (2009)
7. Shamsaei, N., Fatemi, A.: Effect of microstructure and hardness on non-proportional cyclic hardening coefficient and predictions. Mater. Sci. Eng. A **527**, 3015–3024 (2010)
8. Shamsaei, N., Fatemi, A., Socie, D.F.: Multiaxial fatigue evaluation using discriminating strain paths. Int. J. Fatigue **33**, 597–609 (2011)
9. Shamsaei, N., Fatemi, A., Socie, D.F.: Multiaxial cyclic deformation and non-proportional hardening employing discriminating load paths. Int. J. Plast. **26**, 1680–1701 (2010)
10. Meggiolaro, M.A., Castro, J.T.P.: An improved multiaxial rainflow algorithm for non-proportional stress or strain histories—part I: enclosing surface methods. Int. J. Fatigue **42**, 217–226 (2012)
11. Meggiolaro, M.A., Castro, J.T.P.: Prediction of non-proportionality factors of multiaxial histories using the moment of inertia method. Int. J. Fatigue **61**, 151–159 (2014)
12. Kanazawa, K., Miller, K., Brown, M.: Cyclic deformation of 1% Cr–Mo–V steel under out-of-phase loads. Fatigue Fract. Eng. Mater. Struct. **2**, 217–228 (1979)
13. Bishop, J.E.: Characterizing the non-proportional and out-of-phase extend of tensor paths. Fatigue Fract. Eng. Mater. Struct. **23**, 1019–1032 (2000)

14. Mandel, J.: Cours de Mécanique des Milieux Continus, Tomes I and II. Gauthier-Villars, Paris (1966)
15. Tanaka, E.: A nonproportionality parameter and a cyclic viscoplastic constitutive model taking into account amplitude dependences and memory effects of isotropic hardening. Eur. J. Mech. A/Solids **13**, 155–173 (1994)
16. Kida, S., Itoh, T., Sakane, M., Ohnami, M., Socie, D.F.: Dislocation structure and non-proportional hardening of type 304 stainless steel. Fatigue Fract. Eng. Mater. Struct. **20**, 1375–1386 (1997)
17. Jiang, Y., Sehitoglu, H.: Modeling of cyclic ratchetting plasticity, part I: development of constitutive relations. ASME J. Appl. Mech. **63**, 720–725 (1996)
18. Jiang, Y., Sehitoglu, H.: Modeling of cyclic ratchetting plasticity, part II: comparison of model simulations with experiments. ASME J. Appl. Mech. **63**, 726–733 (1996)